Icarus 227 (2014) 78–88

Contents lists available at ScienceDirect

Icarus

journal homepage: www.elsevier.com/locate/icarus

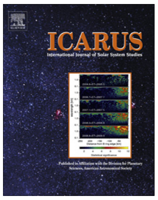

Numerical simulations of ion and electron temperatures in the ionosphere of Mars: Multiple ions and diurnal variations

Majd Matta [a,*], Marina Galand [b], Luke Moore [c], Michael Mendillo [a], Paul Withers [a]

[a] Astronomy Department, Boston University, 725 Commonwealth Ave., Room 514, Boston, MA 02215, United States
[b] Space and Atmospheric Physics Group, Imperial College London, South Kensington Campus, London SW7 2AZ, United Kingdom
[c] Center for Space Physics, Boston University, 725 Commonwealth Ave., Room 506, Boston, MA 02215, United States

ARTICLE INFO

Article history:
Received 5 June 2013
Revised 19 August 2013
Accepted 7 September 2013
Available online 21 September 2013

Keywords:
Mars
Ionospheres
Atmospheres, dynamics

ABSTRACT

This study shows how ion and electron temperatures in the ionosphere of Mars, which affect plasma densities, vary with altitude and time of day. These new results can be used to support the interpretation of existing and anticipated measurements of ionospheric conditions. Here, a one-dimensional fluid model of the martian ionosphere has been coupled to a kinetic supra-thermal electron transport model in order to self-consistently calculate ion and electron densities and temperatures. The models include diurnal variations, revealing hundreds of degrees Kelvin changes in dayside electron and ion temperatures at fixed altitude. The models treat each ion species separately, revealing hundreds of degrees Kelvin differences between H^+ and O_2^+ temperatures. The coupled models also include an adiabatic expansion term into the heating equation, which contribute significantly to temperatures of lighter ions. Consistent with previous studies using single-ion plasma, solar EUV heating alone is insufficient to heat the thermal electrons and ion species to observed temperatures, indicating the presence of additional heating sources. Best agreement with measurements is found when additional topside heating fluxes of 15×10^9 and 2×10^7 eV cm^{-2} s^{-1} produce topside heating rates that are 35 and 100 times higher than the nominal solar heating rate for electrons and ions, respectively.

1. Introduction

Solar soft X-ray and Extreme Ultra Violet (EUV) photons ionize a fraction of the neutral atmosphere of a planet. Resulting photoelectrons and secondaries produced by electron-impact ionization with energies in excess of their surroundings, referred to as the supra-thermal electron population, ionize neutral species further or heat up the ambient plasma. Thermal electrons that are heated by the supra-thermal electron population cool down through interactions with colder ions and neutrals. Heat exchanged between ions and other particles occurs through collisions. This fundamental heating process drives plasma temperatures in ionospheres. For some planets and moons, precipitating particles or solar wind interactions at the upper boundary of the ionosphere can introduce additional heating sources to the local plasma.

The thermal structure of plasma can affect ion chemistry and dynamics. Several chemical reaction rates have direct or inverse plasma temperature dependence (Anicich, 1993; Schunk and Nagy, 2009). For example, molecular ions recombine with cooler electrons more readily than with hotter ones, affecting production and loss in the photo-chemically dominated region of the ionosphere. In diffusion-dominated regions, plasma scale height is directly proportional to ion and electron temperatures. Hotter plasma diffuses into higher altitudes and this impacts its likelihood for escape. Characterizing the ion and electron temperatures accurately is important for these processes that consequently affect ionospheric structure and dynamics.

The present state of the thermal structure of electron and ion temperatures at Mars is poorly understood. In 1976, the two Viking Landers (VL1 and VL2) each carried a Retarding Potential Analyzer (RPA) for the purpose of measuring plasma density, temperature and velocity with altitude (Hanson et al., 1977). The ion plasma properties derived from the *in situ* measurements of each Lander were in agreement. Only the first Lander provided useable electron temperature measurements due to contamination of the second Lander's instrument (Hanson and Mantas, 1988). Retrieving electron temperature values from the VL1 RPA measurements involved complex analysis and results were published over a decade later (Hanson and Mantas, 1988).

The VL data analysis assumed a basic ionospheric chemistry and measured densities of three ion species at Mars (O_2^+, O^+ and CO_2^+), all of which were assumed to have the same temperature. Measurements of ion temperature and density profiles extended

---

* Corresponding author.
E-mail addresses: majdm@bu.edu (M. Matta), m.galand@imperial.ac.uk (M. Galand), moore@bu.edu (L. Moore), mendillo@bu.edu (M. Mendillo), withers@bu.edu (P. Withers).

0019-1035/$ - see front matter © 2013 Elsevier Inc. All rights reserved.
http://dx.doi.org/10.1016/j.icarus.2013.09.006

between 120 km and ~300 km and showed a steadily increasing ion temperature with increasing altitude from ~200 K at 150 km to ~2500 K at 300 km. The electron temperature profile obtained from the VL1 RPA measurements could only be retrieved between 215 and 330 km and had an average value of ~3000 K (Hanson and Mantas, 1988). The lack of additional *in situ* measurements of plasma temperatures at Mars has led the ionospheric modeling community to adopt smoothed and extrapolated functional forms of the VL1 measurements as the appropriate input parameters for subsequent modeling efforts (e.g., Fox et al., 1996).

Theoretical calculations of plasma temperatures at Mars began soon after the Mariner 4 flyby (Henry and McElroy, 1968; Shimizu and Ashihara, 1972). Following the publication of VL1 ion temperatures at Mars, several models were developed to reproduce the measurements and to estimate electron temperature profiles (e.g. Choi et al., 1998 and references therein). Despite their nuances, all models assumed a basic chemistry that used the Viking Lander measured neutral atmosphere and generated the three ion species determined by the VL1 RPA (Nier and McElroy, 1976; Hanson et al., 1977). The models unanimously agreed that solar EUV heating alone could not account for the high ion temperature measured at Mars. It was concluded that either external heating sources were supplied to the plasma by combinations of wave dissipation, chemical and Joule heating, or that a slightly inclined magnetic field (just off horizontal) was inhibiting the vertical motion that leads to conductive cooling of plasma (Chen et al., 1978; Johnson, 1978; Rohrbaugh et al., 1979; Cravens et al., 1980; Singhal and Whitten, 1988; Choi et al., 1998).

Most models that calculated martian plasma temperatures ran steady-state simulations to reproduce the measurements made for VL1 conditions. Only one study to date published diurnal ion and electron temperature values and did so at 350 km altitude only (Singhal and Whitten, 1988). As was done for the VL data analysis, these models assumed that all ions had the same temperature.

Recent studies incorporated H and H_2 into the makeup of the martian neutral atmosphere and found that the composition of the ionosphere of Mars can have varying levels of hydrogenation that yield ion species more diverse than the three ions determined by the RPAs (Krasnopolsky, 2002; Fox, 2003; Matta et al., 2013). In light of these results, the present study addresses the following two questions: (1) What are the temperatures of different ion species at Mars? and (2) What are the local time variations of the ion and electron temperatures at various ionospheric altitudes?

In this work, a comprehensive implementation of the energy equation is used to simulate plasma temperatures. This approach derives multi-species ion temperatures and models the variation in plasma temperatures as a function of altitude and local time for the first time at Mars. The effects of multiple ion interactions are analyzed and discussed. Comparisons are made with VL1 measurements as well as with results of other models that have been run at similar conditions.

A brief description of the model used for plasma temperature calculations is described in Section 2. Resulting temperatures are shown and compared to VL1 measurements in Section 3 then discussed and compared to other models in Section 4. The conclusions of this work are given in Section 5. Equations and assumptions specific to the energy calculations are detailed in the Appendix.

2. Model description

This work uses a one-dimensional fluid model of the martian ionosphere. This model is described at length in Mendillo et al. (2011) and Matta et al. (2013). In brief, the model takes as input a neutral atmosphere (CO_2, O, CO, N_2, Ar, H and H_2), solar flux, photo-absorption and photo-ionization cross-sections, chemical reaction and recombination rates, and for initial conditions, parameterizations with altitude of electron-impact ionization rates and plasma temperatures. The model for this study solves the coupled continuity and momentum equations for ion and electron densities as well as for ion velocities. It is time-dependent, and so output parameters are generated as a function of altitude as well as local time.

In order to use this ionospheric model to solve for plasma temperature, the energy equation was incorporated into the simulation. The fluid model was then used in conjunction with an energy deposition model adapted from Venus (Cui et al., 2011) to Mars. This energy deposition is derived from two coupled modules. The first one solves the Beer–Lambert law to calculate the absorption of solar photons from the top of the atmosphere down to the homopause, and generates the photo-production rate of each ion species. The second module solves the Boltzmann equation applied to supra-thermal electrons. This describes the transport, energy degradation and pitch angle redistribution of photo-electrons and their secondaries. It calculates the electron-impact ionization rates, as well as the thermal electron heating rate due to Coulomb collisions between supra-thermal and thermal electrons. The coupling of the energy deposition and ionospheric models facilitates self-consistent calculations of thermal heating rates, primary and secondary electron and ion production rates as well as electron and ion temperatures, similarly to Moore et al. (2008) for Saturn. For the purpose of using these models, the wavelength resolution of solar flux as well as the cross-section input to the fluid model was upgraded from 39 wavelength bins to 1 nm bin resolution spanning 0.5 to 125.5 nm (Woods et al., 2005; Tobsika and Bouwer, 2006).

The 1-D representation along the vertical direction of the 5th-moment energy equation used in the model assumes multi-species partially ionized plasma (Schunk and Nagy, 2009):

$$\frac{3}{2}n_s k_B\frac{\partial T_s}{\partial t} = \underbrace{\sin^2 I\frac{\partial}{\partial z}\left(\lambda_s\frac{\partial T_s}{\partial z}\right)}_{\text{CONDUCTION}} + Q_s - \sum L_s - \underbrace{n_s k_B T_s \sin^2 I\frac{\partial v_s}{\partial z}}_{\text{ADIABATIC EXPANSION}} - \underbrace{\frac{3}{2}n_s k_B v_s \sin^2 I\frac{\partial T_s}{\partial z}}_{\text{ADVECTION}} \tag{1}$$

where the subscript s refers to either thermal electron or ion species, n is the electron or ion number density, k_B is the Boltzmann constant, T is the electron or ion temperature, t is time, I is the inclination angle of the magnetic field from the horizontal and is taken to be 90° for cases of no fields, z is altitude, λ is the electron or ion coefficient of thermal conductivity and v is electron or ion velocity. The first term on the right hand side represents the effects of conductivity on energy flow. The second term is the heating rate, Q. The electron heating rate comes from energy transfer due to Coulomb collisions from the supra-thermal photo-electrons and their secondaries. The ion heating rate comes from collisional heat transferred from electrons. The third term is the sum of all cooling rates, L, due to elastic and non-elastic collisions with charged and neutral particles. The fourth and fifth terms represent thermal contributions of adiabatic expansion and advection, respectively.

The plasma density and velocity profiles are derived by solving the coupled continuity and momentum equations. The electron heating rate is supplied by the kinetic electron transport code driven by the thermal electron number density and temperature calculated by the ionospheric model. The initial plasma temperatures are set equal to the neutral temperature for all local times at a fixed location. The only energy source considered is solar radiation. The full diurnal output from the ionospheric model using these initial conditions is used as input into the kinetic model that generates the supra-thermal heating rate for all local times. This diurnal heating rate is then fed back into the ionospheric model and used to solve for plasma temperatures self-consistently. The subsequent cooling and heating rates are species-specific and are derived from expressions listed in the Appendix. The kinetic and fluid models iterate their output until satisfactory convergence (to within ~5%) is reached in all output parameters for all altitudes and local times. This convergence typically occurs after three iterations.

The neutral temperature profile was assumed to be fixed in local time, and so, a few conditions were imposed on the temperature calculations in the ionospheric model. Both the electron and ion temperatures were constrained to have the neutral temperature as a minimum value at each altitude to prevent the thermal conductivities from cooling the electron and ion temperatures below the neutral temperature. To maintain numerical stability within the simulation the electron (ion) temperature below 110 (130) km was set to be equal to the neutral temperature at all local times. Below 110 km, the electron temperature is not expected to diverge significantly from the neutral temperature due to large electron–neutral collision frequencies. Both the electron and ion temperature gradients were set to zero at the top boundary. The altitude of the top boundary in the model is 400 km. Enforcing a zero-gradient top boundary condition several scale heights above the topmost altitude of interest (300–350 km) contributed to the numerical stability of the calculations without affecting the validity of the calculations.

A solar minimum flux ($F_{10.7} = 68$), a Sun–Mars distance of 1.64 AU, a solar declination of 15° and a surface latitude of 23° are used in this work resulting in an ionosphere with a solar zenith angle (SZA) of ~44° at 3 pm Local Time (LT). These specifications reproduce the Viking Lander 1 entry conditions that are used to simulate the diurnal plasma temperature as a function of altitude and time over one martian day (Sol). In the time span of one Sol, the model conditions for Sun–Mars distance, neutral atmosphere (densities and temperature both derived from the Mars Climate Database (Forget et al., 1999; Lewis et al., 1999)), solar longitude and declination are taken to be fixed. No magnetic fields are assumed at this location, consistent with the measurement conditions. Calculations are therefore performed along the local vertical.

3. Results

3.1. Electron temperature for VL1

The nominal model electron temperature profile for the Viking Lander 1 conditions is shown along side the measured electron temperature and the MCD-derived neutral temperature profiles in Fig. 1. The neutral temperature is 204 K above 200 km. Between 215 and 300 km, the VL1 electron temperature varies between 2240 and 5440 K with a sharp increase to ~7100 K at 225 km. The model electron temperature profile varies by nearly an order of magnitude between the lower and upper altitude boundaries. Electrons below 110 km are constrained to the neutral temperature values. At 110 km, the electron temperature deviates from the neutral temperature value of ~137 K to reach 1130 K at 160 km. This warming is due to the photo-electron heating rate that reaches a maximum in this altitude region where the ionization rate due to solar EUV is at its peak.

Above 160 km, the electron temperature increases much more slowly with altitude, reaching ~1360 K at 300 km. At higher altitudes, the photo-ionization rates decrease and so, the solar heating rate decreases allowing the electron thermal conductivity to dominate and ensure a near-isothermal profile.

The smoothed measured electron temperatures (~3000 K above 215 km from the dotted line in Fig. 1) are nearly a factor of 2 larger than those predicted by the model (solid line in Fig. 1). This could be attributed to a shortfall in the model that misses a heating source for electrons (e.g., from interactions with the solar wind, dissipating waves or energetic particles), or could be due to uncertainties in the data. An elaborate discussion of the reliability of the VL1-derived electron temperature concluded that the interpretations of the RPA measurements are not uniquely determined (Mantas and Hanson, 1979, 1985, 1987; Hanson and Mantas, 1988). The fitting function used to extract electron temperature from the current–voltage measurements on the RPA was one of several solutions that approximated the sensor geometry (Hanson and Mantas, 1988). Our model electron temperatures are consistent with those found by other workers for similar conditions (see Sections 4.4 and 4.5) and thus we assume, as others did, that the discrepancy between modeled and observed results was due to additional heating sources.

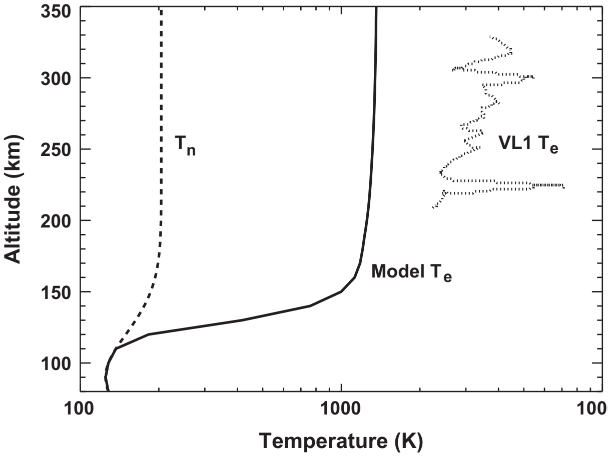

Fig. 1. Modeled electron temperature T_e profile (solid line) for VL1 conditions: 44° SZA, low latitude, solar minimum. The dashes represent the neutral temperature T_n derived from the Mars Climate Database (MCD) (Forget et al., 1999) and the dotted line is the measured electron temperature from Viking Lander 1 (Hanson and Mantas, 1988).

3.2. Ion temperature for VL1

Our model generates and tracks 16 ion species, the most dominant of which is O_2^+ below 350 km (Matta et al., 2013). The heating rate for ions has a mass-dependence resulting in lighter ion species (e.g., H^+) being heated more efficiently than heavier ones. A 16-ion solution to the energy equation is used to generate an individual temperature profile for each ion species. The resulting ion temperature profiles for VL1 conditions are shown in Fig. 2.

Two mass groups of ion species have similar temperature trends as can be seen in Fig. 2. The lightest ion group has masses between 1 and 3 amu and reaches temperatures between ~570 and ~760 K at 300 km. These ions consist of H^+, H_2^+ and H_3^+ (shown in Fig. 2 in gray, orange and blue, respectively) and will be referred to hereafter as the H^+ ion group. A second heavier group of ion species with masses between 16 and 45 amu is well thermalized to its constituents and reaches a temperature of ~525 K at 300 km. Although all 16 ion temperatures are calculated independently, the temperatures of the 13 ions in the heavy ion group are found to have the same modeled temperature profile shown in red in Fig. 2 to within 1%. These heavier ions will be referred to as the O_2^+ group since this ion species is the dominant one in the martian ionosphere.

Ions in both groups display similar thermal behavior with altitude. Below 130 km, the ion temperatures are the same as the neutral temperature due to the lower boundary conditions described

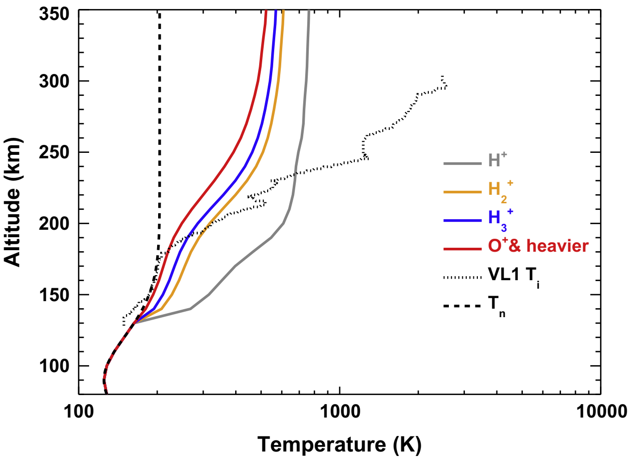

Fig. 2. Ion temperature profiles T_i modeled for VL1 conditions for 16 ion species shown in solid colors. The dashes represent the neutral temperature T_n from the MCD (Forget et al., 1999) and the dotted line is the Viking Lander 1 ion temperature (Hanson et al., 1977). Ions with masses heavier than 16 amu ($OH^+, N_2^+, CO^+, N_2H^+, HOC^+, HCO^+, NO^+, O_2^+, Ar^+, ArH^+, CO_2^+$ and HCO_2^+) were found to have the same modeled temperature profile shown for O^+.

in Section 2. Ion temperatures diverge from the neutral temperature at ~130 km, with a larger departure for the lighter ions. This occurs at altitudes where the ion heating term dominates. A second temperature increase occurs near 210 km for the O_2^+ group and near 170 km for H^+ that is due to the dominance of the ion thermal conductivity term at those altitudes. At 210 km, ion temperatures vary by over 370 K due to their mass diversity, reaching values between ~270 and 640 K for VL1 conditions.

The VL1 and VL2 thermospheric measurements were made at similar solar zenith angles and during the same solar activity. Both ion temperature measurements had similar profiles and increased above 180 km to reach ~2500 K at 300 km. These measurements were interpreted assuming all three measured ions (CO_2^+, O_2^+ and O^+) had the same temperature. The model shows that these three ions have the same temperature as well to within 1%.

The modeled ion temperatures agree well with VL1 measurements below 180 km. Between 180 and 230 km, the model heavy and light group ion temperatures bracket the observed values. The temperature derived for all ion species recreates the trend seen in the observations for increased values at 150 km and ~200 km. Above 230 km, the observed temperatures continue to increase to reach ~2470 K at 305 km while model values increase much slower to reach temperatures that are cooler by about a factor of 4 at top altitudes. Increasing the electron temperature to the VL1 observed values does not resolve the differences above 200 km between the calculated and observed ion temperatures. Additional heating mechanisms for ion species are still required for their model temperatures to reproduce observations.

The vertical gradient in ion temperature is smaller than for the electron temperature resulting in a relatively smaller contribution from the ion thermal conductivity on temperature structure. At high altitudes, the ion temperatures become isothermal due to the balancing of heating and cooling from collisions with warmer particles (typically electrons) and cooler particles (typically neutral or other ion species), respectively.

3.3. Plasma densities for VL1

The next modeling task is to seek validation via comparisons with basic ionospheric morphology observed by VL1. The plasma temperatures and densities are calculated self-consistently in the model. Fig. 3 shows the modeled electron as well as CO_2^+, O_2^+ and O^+ ion density profiles for the Viking Lander 1 conditions compared with measurements. The results from two simulations are shown. Model DF refers to a simulation where photochemistry and vertical diffusion occur. Model PC refers to a simulation where photochemistry only occurs.

There is good agreement between modeled and measured electron density values between the peak and 200 km. Above 200 km, the photochemical and diffusion model electron densities begin to diverge and neither model results agree with the electron density measurements at high altitudes. The measured O_2^+ density profile is adequately reproduced by the model above the peak through 200 km for the diffusion simulation and through 250 km for the photochemical only simulation. The overall shape of the modeled O^+ density profile above 180 km agrees with measurements for both simulations. The modeled CO_2^+ densities capture the peak altitude and reproduce the trends in measured densities.

The model agreement with measurements is not expected to be exact. Interpretation of VL1 RPA current–voltage measurements required *a priori* knowledge of the species being detected and the resulting ions selected were those plotted in Fig. 3b–d. The model includes comprehensive chemistry that includes species produced by interactions with neutral hydrogen leading to the production of HCO^+ and HCO_2^+ that have larger number densities than O^+ and CO_2^+ at some altitudes (Matta et al., 2013).

The model reproduces the altitude and density of the main electron (M2) peak as well as the electron density and scale height of the ionosphere above the peak up to 200 km. The lower measured densities with respect to the modeled values above 200 km are likely due to horizontal transport effects that are beyond the scope of a 1-D model to reproduce. These effects are discussed further in Section 4.6. From Fig. 3, the measured plasma densities are better reproduced by the photo-chemical model in which vertical diffusion is suppressed.

The electron density profile resulting from this simulation in which the plasma temperatures were calculated self-consistently from solar-photon heating had a peak density that was ~20% larger and a peak altitude that was ~5 km higher than a profile in which the electron, ion and neutral temperatures were all equal to the neutral temperature at the VL1 conditions. This stresses the importance of plasma temperature effects on ionospheric properties in regions that are in photo-chemical equilibrium.

3.4. Plasma temperature with local time

The model used in this work is time-dependent and can resolve plasma temperature output as a function of time. The resulting diurnal electron temperature map is calculated for the first time for all ionospheric altitudes and shown in Fig. 4. Diurnal ion temperature maps of both light and heavy ion groups are shown in Fig. 5. The electron (ion) temperature does not diverge from the neutral temperature below 110 (130) km at all local times, due to the imposed lower boundary conditions.

These results are characteristic of solar minimum at low latitudes. At these conditions, sunset occurs at 8 pm local time where the SZA $\geqslant$ 110°. At nighttime, the plasma temperature quickly cools down to the neutral temperature and remains there until sunrise. At high altitudes, the electron temperature diverges from the neutral one to reach values of ~1400 K at noon, while O_2^+ and H^+ temperatures reach maximum values at noon-time of ~540 and 780 K, respectively.

The simulations have shown that, soon after sunset, plasma temperatures quickly drop to the neutral temperature values (constrained to be the minimum value). During nighttime, the plasma densities decrease from few 10^{-2} cm^{-3} to few 10^{-1} cm^{-3}. The contribution of these small nighttime plasma density values to the

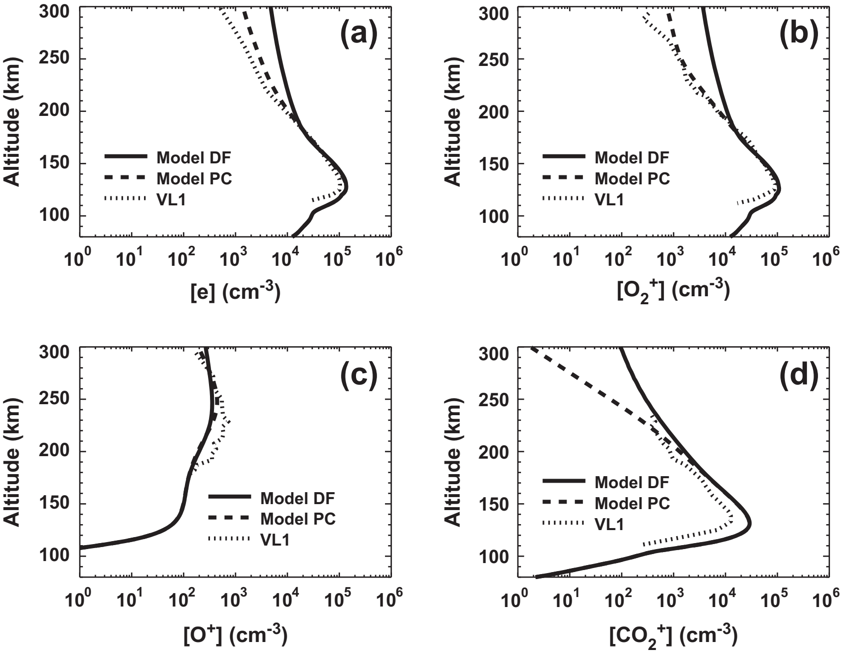

Fig. 3. Comparison of the VL1 RPA plasma number density measurements (dotted lines) with modeled plasma number density profiles for VL1 conditions for (a) electrons, (b) O_2^+, (c) O^+ and (d) CO_2^+. Model DF results shown in solid lines are for a photochemical plus vertical diffusion simulation. Model PC results shown in dashed lines are for a photochemical only simulation.

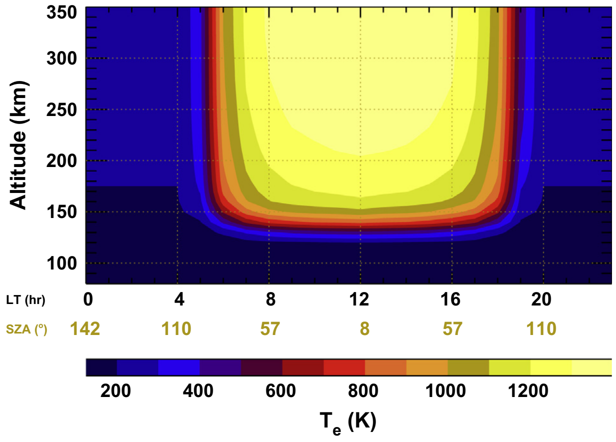

Fig. 4. Diurnal map of modeled electron temperature as a function of altitude and local time for solar minimum low-latitude conditions. Resulting temperatures are calculated due to solar photon heating only. Dotted lines are shown at 4 h and 50 km increments for clarity.

daytime ionosphere is negligible. Suppressing the nighttime calculations of plasma temperatures – when all ion species are thermalized to the neutral species and electron concentrations are very small – did not change the outcome of daytime temperatures or densities. This method was adopted to improve simulation run times without loss of model accuracy.

4. Discussion

4.1. Multi-ion effects

Lighter ions, such as H^+, H_2^+ and H_3^+, make up a minority of the total plasma density at Mars but their effects on heavier ion energies can be substantial. A multi-ion vs. single-ion treatment of calculating ion temperatures had negligible effects on electron temperature calculations (<3% at all altitudes and local times). Ion temperature calculations, however, were significantly affected by the presence of other hotter or colder ions.

Chen et al. (1978) accounted for H^+ in simulations of ion composition and assumed all ions had the same temperature. A more recent investigation showed that between 150 and 250 km the temperature of H^+ was warmer than that of O_2^+ when calculated separately (O. Witasse, 2013, personal communication). Our results confirm this finding and provide a detailed assessment of individual ion temperatures.

The ion heating rate is inversely dependent on ion mass while the cooling rate is inversely dependent on the square root of ion mass (see Appendix). A light ion such as H^+ heats up 32 times faster than O_2^+ and loses heat only 5.6 times faster. Consequently, lighter ions are heated more efficiently by supra-thermal electrons before reaching thermal equilibrium. Individual ions are subject to heating by lighter ion collisions as well as to cooling by heavier ion collisions, thus a multi-ion treatment to temperatures provides added heating and cooling mechanisms for ions.

Results from a simulation where only O_2^+ heating occurs and all ions are assumed to have the same temperature were compared with a simulation where O_2^+ is independently heated along with 15 other ions. The inclusion of multi-ion heating resulted in an O_2^+ plasma that was a factor of 2 cooler, since it collisionally shared its energy with other ions.

4.2. Electron energy terms

Models that calculate plasma temperatures at Earth, Mars and sometimes Venus often ignore advection and adiabatic expansion terms for both electrons and ions (e.g., Herman et al., 1971; Choi et al., 1998; Schunk and Nagy, 2009). These assumptions are valid for many terrestrial regions, but not for ionospheres of other bodies such as Venus and Titan where ion species develop significant vertical ion velocities (e.g., Chen and Nagy, 1978; Roboz and Nagy, 1994). In this work, all the energy terms are included and their

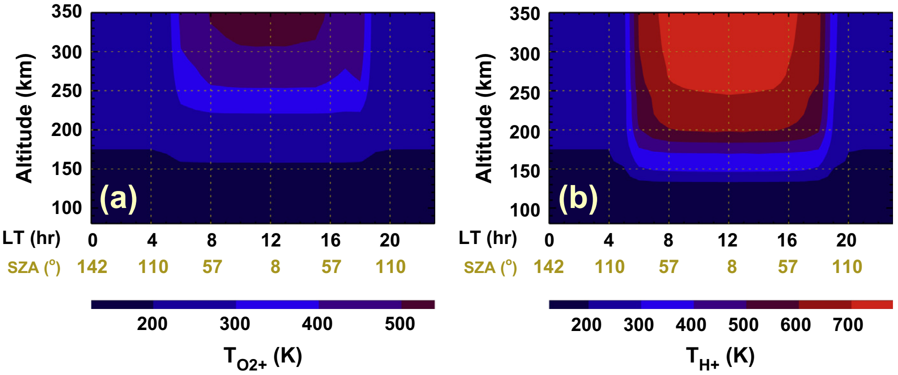

Fig. 5. Diurnal map of modeled ion temperatures of (a) O_2^+ and (b) H^+ ion groups as a function of altitude and local time for solar minimum low-latitude conditions. The ion temperatures are calculated due to collisions with thermal electrons that are heated by solar photons only. Dotted lines are shown for clarity as in Fig. 4.

individual contributions to temperature calculations are evaluated for electrons and both representative groups of ion species.

Contributions from each term in the thermal electron energy equation are shown in Fig. 6 for the VL1 conditions. The advection and adiabatic expansion terms were found to contribute by less than 0.1% to electron energy calculations at all local times and can be neglected.

Solar EUV photons deposit most of their energies at and around the M2 peak (~130 km), and so, this is the altitude of peak photoionization as well as of peak heating for the thermal electron gas. Cooling of thermal electrons occurs as a result of elastic and inelastic interactions with neutrals, dominated by CO_2 rotation (see Appendix), and peaks at the altitude where the product of electron density and CO_2 densities are the highest in the regions where most of the solar EUV is absorbed (also at ~130 km). The electron thermal conductivity term provides an effective cooling mechanism that conducts the heat downward in altitude above 140 km from regions of higher temperature to regions of cooler temperature and balances the heating at higher altitudes.

4.3. Ion energy terms

In the plasma-dense region below 150 km, heating and cooling due to collisions with hotter and colder particles, respectively, dominate thermal balance for all ion species. As a result, ion heating and cooling rates each peak at altitudes of maximum electron density. At higher altitudes, the remaining energy terms become more important. Fig. 7 shows the contribution of the various terms in the energy equation focusing on the two representative ion species in the altitude range above 150 km.

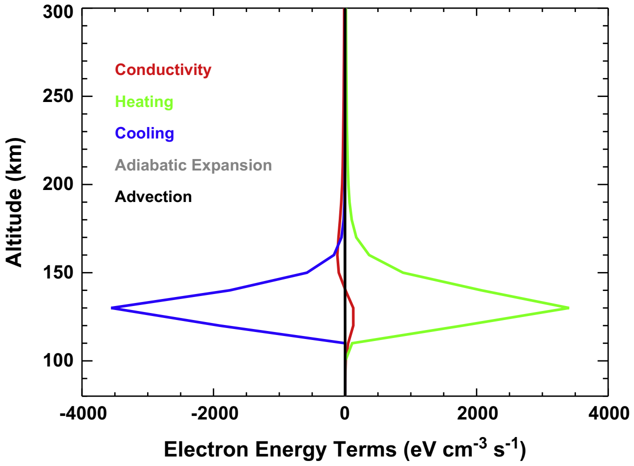

Fig. 6. Modeled electron energy terms from Eq. (1) at noon for solar minimum low-latitude conditions. Conductivity (red line), solar heating (green line), collisional cooling (blue line), adiabatic expansion (gray line) and advection (black line) terms are shown for comparison. The adiabatic expansion profile is barely discernable behind the advection profile.

Conductivity, adiabatic expansion and advection terms can be ignored for heavier ions. However, conductivity and adiabatic expansion provide non-negligible heating and cooling contributions for lighter ones that can exceed the heating rates at lower altitudes. Their effects on thermal balance appear at high altitudes as a result of more prominent ion velocity and temperature gradients in that region. These gradients are more pronounced for ions with smaller masses.

4.4. Validation to observations and other models

With only one *in situ* measured profile of electron temperature and two of ion temperature at Mars, validation of modeled values can be challenging. The modeled electron temperatures in this work are about a factor of two smaller than the averaged VL1 RPA interpreted values between 215 and 300 km (see Section 3.1). Modeled ion temperatures cover a range that brackets the measured ion temperature up to 235 km (see Section 3.2).

The results of ion and electron temperatures derived in this work are compared to those of other models for similar conditions; namely, Viking Lander 1 local conditions with only solar EUV heating. Table 1 compares measured and modeled electron and ion temperatures at 250 km, the altitude above which the modeled electron temperature becomes nearly isothermal. Differences in temperature values between our model and others shown in the table are likely due to minor differences in model input and to more substantial differences in assumptions. Some of the key assumptions made by other models are that all ions have the same temperature, that advection and adiabatic expansion are negligible for all species, and that the heating or cooling due to thermal conductivity is reduced by the effects of ad hoc magnetic field inclinations.

The range of ion temperatures found in this work and provided in Table 1 corresponds to the range of ion species in the simulations. The O_2^+ ion group reached ~370 K at 250 km and the H^+ ion group reached 680 K.

4.5. External heating effects

Previous studies have shown that separate topside heating fluxes for electron and ion populations are needed in order to bring simulation results of plasma temperatures into agreement with

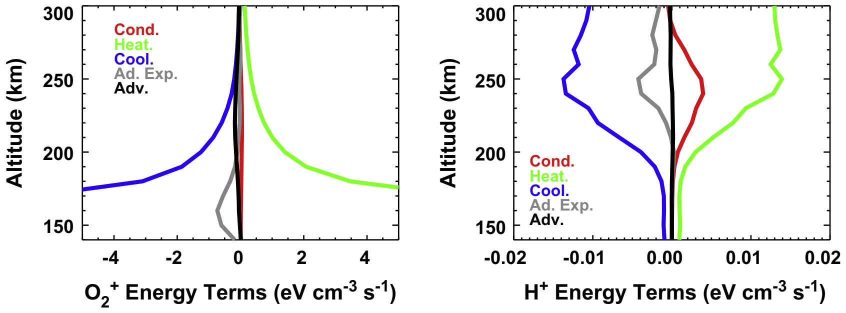

Fig. 7. Modeled ion energy terms from Eq. (1) at noon for solar minimum low latitude conditions. Conductivity (red line), solar heating (green line), collisional cooling (blue line), adiabatic expansion (gray line) and advection (black line) terms are shown for each of the (a) O_2^+ and (b) H^+ ion groups.

Table 1
Plasma temperatures T_e and T_i at 250 km for solar minimum conditions. Model values are derived using solar EUV heating as the only energy source.

T_e (K)	T_i (K)	Source
–	1230	Measurements: Hanson et al. (1977)
3350	–	Measurements: Hanson and Mantas (1988)
500	–	Model: Shimizu and Ashihara (1972)
1300	300	Model: Chen et al. (1978)
–	210	Model: Rohrbaugh et al. (1979)
1050	300	Model: Singhal and Whitten (1988)
400	200	Model: Choi et al. (1998)
1320	370–680	Model: This work

measurements for the Viking Lander 1 conditions. These fluxes are summarized in Table 2 for various models. External heating sources were mainly attributed to solar wind interactions (Chen et al., 1978; Johnson, 1978; Rohrbaugh et al., 1979; Choi et al., 1998). Others proposed Joule heating of ions near 200 km (Chen et al., 1978; Johnson, 1978), and chemical heating due to exothermic reactions that generated the dominant ion, O_2^+ (Rohrbaugh et al., 1979). Predating publication of electron temperature measurements at Mars, a top side heating flux was already added to the thermal electrons to determine an electron temperature that best modeled VL1 ion densities (Chen et al., 1978; Rohrbaugh et al., 1979; Singhal and Whitten, 1988).

Further modeling revealed that un-physically large ion velocities would be required to provide the proposed Joule heating needed to achieve agreement with measured ion temperatures (Chen et al., 1978). Subsequent experimental results have argued that heating due to the chemical processes producing O_2^+ would not sufficiently account for the flux needed to achieve model agreement with VL1 and VL2 ion temperature measurements (Hunton et al., 1991; Walter et al., 1993). Despite the relative agreement across several models of requiring an additional heating flux, no consensus has been reached to justify any one heating source.

Separate topside heating fluxes were added to the electron and the O_2^+ ion populations in the model to study the effects of external heating at the topside boundary. The topside heating flux is a boundary condition that is imposed on the $\lambda \times \partial T/\partial z$ portion of the conductivity term. This quantity is then differentiated with altitude to provide a cooling/heating rate equivalent that propagates downward in altitude with no additional heating imposed on any altitude other than the top.

Table 2
Topside heating fluxes ϕ_i and ϕ_e added to ion and electron populations, respectively, to achieve best agreement with VL1 temperature measurements.

ϕ_i (eV cm^{-2} s^{-1})	ϕ_e (eV cm^{-2} s^{-1})	Source
2.5×10^7	30×10^9	Chen et al. (1978)
0.6×10^7	0.5×10^9	Rohrbaugh et al. (1979)
0.42×10^7	0.35×10^9	Singhal and Whitten (1988)
0.36×10^7	4×10^9	Choi et al. (1998)
2×10^7	15×10^9	This work

It was found that simultaneously adding topside heating fluxes of 15×10^9 eV cm^{-2} s^{-1} and 2×10^7 eV cm^{-2} s^{-1} to the electron and O_2^+ populations, respectively, resulted in plasma temperatures that agreed best with the VL1 measurements. The same topside fluxes were applied at all local times in the model. Modeled electron and ion temperature profiles were sensitive to changes of less than a factor of 2 in the topside fluxes. A *t*-test at the confidence level $\geqslant$95% showed that there is no difference between the data and model means at overlapping altitudes. The resulting temperature profiles are shown in Fig. 8. The flux values provided in this simulation are within the range of values applied by previous studies as listed in Table 2.

There are no indications in the literature to the accuracy of the electron temperature spike near 225 km reaching ~7100 K, and it has generally been smoothed out in functional representations of electron temperature (e.g., Fox et al. (1996)). In a simulation where a topside heating flux is applied only to electrons, the resulting electron temperature has a smoothly increasing profile and requires 20×10^9 eV cm^{-2} s^{-1} to match the overall trend from observations (blue profile in Fig. 8a). Similarly, in a simulation where a topside heating flux is applied only to ions, the resulting ion temperature has a smoothly increasing profile and requires a flux of 2×10^7 eV cm^{-2} s^{-1} to match observations (red profile in Fig. 8b). The corresponding electron temperature (red profile in Fig. 8a) decreased slightly above 230 km with the addition of a topside ion flux due to electrons being slightly less conductive than in the absence of an ion topside flux. In a simulation where a topside heating flux is applied to electrons and ions simultaneously, the electrons required a smaller topside flux (15×10^9 eV cm^{-2} s^{-1}) since they were cooled less by a warmer ion population, and resulted in the formation of a bulge near 190 km (solid black profiles in Fig. 8). The black solid profile in Fig. 8a shows an increasing trend in electron temperature that decreases between 200 and 250 km and then increases again above 250 km. This thermal structure is due to the heating (cooling) rate produced by the electron thermal conductivity that peaks at 160 km (260 km), in addition to the added heating effect at the top boundary due to the addition of topside flux. This trend is consistent with the measured electron temperature profile when the outlying data point at 225 km is considered. The blue profile of Fig. 8a (topside electron heating flux only) agrees with the electron temperature measurements excluding the outlier.

The addition of a topside heating flux changes the relative contributions of the thermal conductivity terms for electrons and ions than their solar-radiation-only counterparts shown in Figs. 6 and

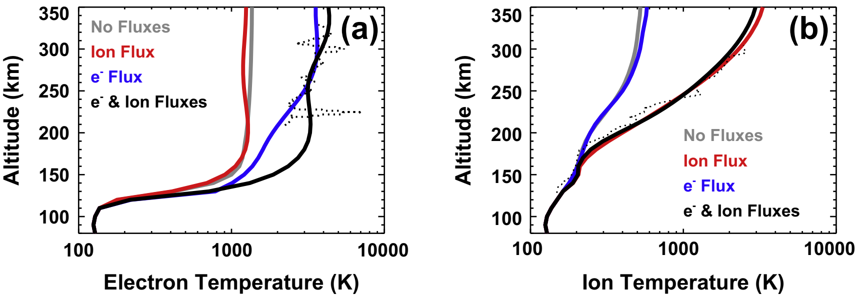

Fig. 8. Model results of (a) electron and (b) ion temperature profiles with additional topside heating flux compared with measurements. Gray lines show model results for no topside heat flux. Red lines show model results when only an ion topside heat flux of 2×10^7 eV cm^{-2} s^{-1} is added. Blue lines show model results when only an electron topside heat flux of 20×10^9 eV cm^{-2} s^{-1} is added. Black solid lines show model results when simultaneous electron and ion topside heating fluxes of 15×10^9 and 2×10^7 eV cm^{-2} s^{-1}, respectively, are added. Dotted black lines show VL1 temperatures.

7a, respectively, and these terms now dominate much of the thermal structure above 150 km. A topside electron heating flux of 15×10^9 eV cm^{-2} s^{-1} produced a heating rate that was 35 times higher than the solar driven heating rate above 300 km and up to 5 times higher between 150 and 200 km. At lower altitudes, the topside flux contributions to heating had diminished to less than the solar EUV heating rate. Similarly for ions, the topside heating flux of 2×10^7 eV cm^{-2} s^{-1} produced an ion heating rate that was 100 times higher than the nominal heating rate for ions at high altitudes and diminished steadily with decreasing altitude.

The addition of topside ion heating flux was only included for the main ion, O_2^+ for comparison to other works. The resulting topside O_2^+ temperatures increased by a factor of 4 from 520 K to ~2100 K (gray profile in Fig. 8b). The remaining ion temperatures also increased by an average of 60% on the topside as a result of collisions with a hotter O_2^+ ion population, despite not having an additional topside flux.

If external heating fluxes occur due to solar wind interaction with the ionosphere, it is likely that the magnitude of the topside heating flux has solar zenith angle and/or location dependencies. Given the lack of available *in situ* measurements of plasma temperatures for various martian conditions, we refrain from parameterizing the diurnal behavior of topside heating fluxes in this work. The upcoming measurements of Mars Atmosphere and Volatile Evolution (MAVEN) instruments of thermal electron and ion distributions down to ~125 km will provide a much larger database of plasma properties to interpret.

4.6. Vertical transport effects

For the Viking 1 Lander conditions, vertical transport becomes important in the ionosphere above 150 km. Below 150 km, vertical plasma motion is restricted by frequent collisions with neutral species, and photochemistry dominates (see Fig. 3a). At Mars, the solar wind creates an induced field region that can penetrate into the upper ionosphere. In regions of weak crustal fields, the induced field has a draped morphology that prohibits vertical transport at altitudes as low as 200 km. An analysis of Viking Orbiter radio occultation profiles showed that the ionosphere can behave photochemically (prohibit upward diffusion), up to 250 km due to the suppression of vertical transport by weak vertical fields and strong horizontal fields (Ness et al., 2000). Our model results demonstrate this in the more favorable agreement of measured ion densities with the photochemical-only simulation shown in Fig. 3. VL1 measured horizontal bulk ion velocities that were comparable in magnitude to the vertical diffusion velocities calculated in this model (Hanson et al., 1977). A 1-D photochemical-only solution suppresses vertical transport, but the effects of horizontal transport are still not accounted for. Modeling horizontal effects accurately requires multi-dimensional modeling that we defer to future work.

The Viking 1 Lander made its descent in the northern hemisphere of Mars (22.48°N, 49.97°W), where crustal magnetic fields are weak. Ionospheric plasma and the local crustal field together act to oppose the solar wind ram pressure. The ionospheric thermal pressure is dominated by the electron plasma component. At the VL1 landing site, the crustal magnetic field pressure is relatively weak and contributes little (<20%) to the total ionospheric pressure at the topside ionosphere (Arkani-Hamed, 2004). For the induced field to inhibit vertical motion for the Viking Lander conditions modeled here, the solar wind would need to have a predominantly horizontal component with an overall magnitude calculated to be ~37 nT at 190 km. This is in agreement with the theoretical values of induced-field magnitude given by Shinagawa and Cravens (1989). MAVEN will be equipped with a magnetometer that promises to resolve differences with model estimates of magnetic field and provide clearer contributions of solar wind interactions *in situ*.

4.7. Model predictions

The composition of the ionosphere of Mars has been recently modeled for solar minimum conditions using the Viking Lander 1 plasma temperatures as input conditions (Matta et al., 2013). In this work, the electron and ion temperatures as well as secondary ionization rates are self-consistently calculated. The resulting ion composition and the vertical diffusion velocities are shown in Fig. 9 for selected ion species.

The inclusion of less than 2 ppm of H_2 at 80 km in the neutral atmospheric composition leads to a significant reduction in O^+ densities above 200 km. Hydrogen is very reactive with the ionosphere of Mars and leads to the production of two stable ions HCO^+ and HCO_2^+.

For all ions, diffusion velocities are negligible below 150 km in the highly collisional and photo-chemically controlled region. At the VL1 conditions modeled here, the lightest ion, H^+, diffuses downwards between 180 and 250 km and reaches a peak speed of 160 m/s at 210 km. H^+ diffuses upwards above 250 km with steadily increasing speeds due to pressure gradients and reaches ~230 m/s at 350 km. Heavier ions, such as O_2^+, diffuse upwards at all altitudes above 150 km with slowly increasing speeds to reach an average of ~80 m/s at 350 km. The heavy ion species (masses $\geqslant 16$ amu) have similar velocity profiles that vary by a few percent above 250 km.

5. Conclusion

A 1-D ionospheric model and an electron transport model have been coupled to derive supra-thermal electron heating rates at Mars due to solar EUV heating. The resulting heating rates were then used to self-consistently calculate plasma temperatures for the Viking Lander 1 conditions.

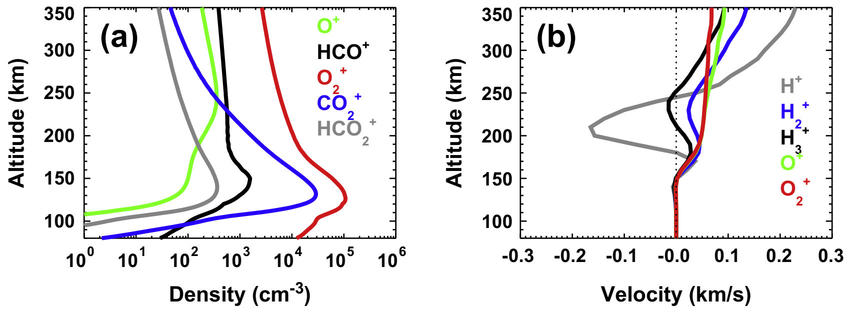

Fig. 9. Model results for composition and diffusion velocities resulting from solar radiation-only heated atmosphere at the Viking Lander 1 conditions. In panel (a), the ion density profiles are shown only for the five most abundant ion species: O_2^+ (red line), CO_2^+ (blue line), HCO^+ (black line), O^+ (green line) and HCO_2^+ (gray line). In panel (b), the ion velocities are shown for selected ion species with a modified color scheme for clarity: H^+ (gray line), H_2^+ (blue line), H_3^+ (black line), O^+ (green line) and O_2^+ (red line). A dotted line shows the zero-velocity region. The remaining ion velocity profiles have been omitted for clarity and occupy the region in between the profiles for O^+ and O_2^+.

This study is the first to calculate ion temperatures at Mars for various ion populations independently. We demonstrate that lighter ion species (e.g. H^+, H_2^+ and H_3^+) at Mars are more effectively heated by the supra-thermal electron population than heavier ones. These lighter ions provide a heating source for heavier ion species.

This work is also the first to demonstrate the importance of the adiabatic expansion energy source on plasma heating at Mars. The non-negligible contribution of this term to ion heating at high altitudes is of particular importance to lighter ion calculations. Low mass ions also have larger transport velocities and are heated more efficiently than heavier ones. Inclusion of this term in energy calculations allows for a broad application of plasma temperature derivation and lays the groundwork for interpretation of MAVEN measurements.

Consistent with previous work, our model temperatures derived from solar radiation heating alone do not agree well with VL1 measurements. Introducing topside heating fluxes to the ion and electron populations resulted in plasma temperatures that better fit the VL1 measurements. The topside fluxes generated an additional heating rate that was 35 (100) times higher than the solar radiation heating rate at 300 km for electrons (ions).

Maps of electron and ion temperature variability with local time and altitude are derived for solar minimum conditions for the first time. In these maps, solar radiation is considered as the only heating mechanism with no external topside heating flux.

The diurnal variability in electron and ion temperatures can impact dependent plasma processes. For example, ionospheric loss at the main peak is predominantly due to the dissociative recombination of O_2^+ at a rate that varies as $T_e^{-0.7}$ (Schunk and Nagy, 2009). This recombination rate, and hence, electron loss near the peak varies by a factor of 2 between local noon and dusk as a result of the diurnal variation of electron temperature at the low-latitude solar minimum conditions modeled here. The O_2^+ recombination rate modeled with self-consistent plasma temperature calculations was a factor of 2 smaller at the peak and a factor of ~4 smaller at higher altitudes than the recombination rate of a simulation in which all temperatures are equal to the neutral temperature.

The model predictions for electron temperature and ion composition and vertical diffusion velocities are relevant to the upcoming MAVEN mission. The model can be used in future work to calculate diurnal plasma temperature maps for various latitudes, solar cycle conditions and martian seasons.

Acknowledgments

The authors would like to thank Professor William Oliver for insightful discussions on numerical modeling and Ingo Müeller-Wodarg for discussions on planetary plasma temperatures. The constructive comments and timely feedback of the reviewers are highly appreciated. This work was supported, in part, by Grants from NSF (AGS-1123222 and AST-1211490) and NASA (NNX08AN56G). MG was partially supported by the STFC Consolidating Grant to the Space and Atmospheric Physics Group at Imperial College London.

Appendix A

The thermal electron energy equation given above (1) is governed by five terms described as conductivity, heating, cooling, adiabatic expansion and advection. Heating rates to the thermal electrons were calculated by a kinetic electron transport model (e.g., Galand et al., 2009). The kinetic electron transport model describes how supra-thermal electrons – such as photoelectrons and their secondaries – are transported in the atmosphere and undergo energy degradation and angular redistribution through collisions with neutral species and thermal electrons. It is based on the solution of the Boltzmann equation applied to energetic electrons applying a multi-stream approach. The model used results from the adaptation of the venusian version to Mars (Cui et al., 2011). Conductivity and cooling rates are required to close the energy equation of each species.

A.1. Electrons

The thermal conductivity of electrons is given by the following expression (Schunk and Nagy, 2009):

$$\lambda_e = \frac{25}{8}\,\frac{k_B p_e}{m_e\left(\nu_{ee} + \frac{13}{8}\sum_i \nu_{ei} + \frac{5}{4}\sum_n \nu_{en} z'_{en}\right)} \tag{A1}$$

where p_e is electron gas pressure, k_B is the Boltzmann constant, m_e is electron mass, ν_{ee}, ν_{ei} and ν_{en} are the weighted electron–electron, electron–ion and electron–neutral collision frequencies, respectively, summed over all species. z'_{en} is a parameter that takes into account the electron–neutral interactions. Assuming a hard–sphere interaction gives $z'_{en} \sim 1$. The expressions for electron–particle collisions are found to be (Schunk and Nagy, 2009):

$$\nu_{ee} = \frac{54.5 n_e}{2^{0.5} T_e^{1.5}} \tag{A2}$$

$$\nu_{ei} = \frac{54.5 n_i}{T_e^{1.5}} \tag{A3}$$

and

$$\nu_{en} = \frac{8}{3\sqrt{\pi}} n_n q_{d-n} \sqrt{\frac{2k_B T_e}{m_e}} \tag{A4}$$

where n_e, n_i and n_n are the electron, ion and neutral densities in cm^{-3}, respectively. T_e is the electron temperature in Kelvin. q_{d-n} is the momentum average collision cross-section in cm^2, given by the following expressions where T_e is in Kelvin ((A5) and (A6) – Schunk and Nagy (1980); (A7) – Henry and McElroy (1968); (A8), (A10), (A11) – Banks and Kockarts (1973); (A9) – Baille et al. (1981)):

$$q_{d-\mathrm{CO_2}} = 4.4 \times 10^{-14} T_e^{-0.5} \left(1 + 4.1 \times 10^{-11} |4500 - T_e|^{2.93}\right) \tag{A5}$$

$$q_{d-\mathrm{CO}} = 2.82 \times 10^{-17} T_e^{-0.5} (165 + T_e) \tag{A6}$$

$$q_{d-\mathrm{O}} = 1.07 \times 10^{-16} \left(1 + 5.7 \times 10^{-4} T_e\right) \tag{A7}$$

$$q_{d-\mathrm{N_2}} = 2.81 \times 10^{-17} T_e^{0.5} \left(1 - 1.21 \times 10^{-4} T_e\right) \tag{A8}$$

$$\begin{aligned} q_{d-\mathrm{Ar}} &= 4.46 \times 10^{-14} T_e^{-0.815} \quad 250 \leqslant T_e \leqslant 600 \\ &= 3.11 \times 10^{-12} T_e^{-1.46} + 2.72 \times 10^{-23} T_e^{1.79} \quad 600 \leqslant T_e \leqslant 1400 \end{aligned} \tag{A9}$$

$$q_{d-\mathrm{H}} = 5.4 \times 10^{-15} \left(1 - 1.35 \times 10^{-4} T_e\right) \tag{A10}$$

$$\begin{aligned} q_{d-\mathrm{H_2}} &= 6.29 \\ &\quad \times 10^{-16} \left(1 + 3.23 \times 10^{-2} T_e^{0.5} - 1.16 \times 10^{-6} T_e^{1.5} - 7.18 \times 10^{-9} T_e^2\right) \end{aligned} \tag{A11}$$

The cooling rate for thermal electrons is governed by the types of interactions in which electrons can dissipate their energy to surrounding species. These can be elastic collisions with neutrals and ions as well as inelastic collisions with neutrals that include rotation, vibration, excitation and fine structure interactions. Hence, cooling processes depend on atmospheric and ionospheric composition. In the model used here, 7 neutral species (CO_2, CO, O, N_2, Ar, H and H_2) and 16 ion species ($CO_2^+, N_2^+, O^+, CO^+, Ar^+, H_2^+, H^+, O_2^+, NO^+, H_3^+, OH^+, HCO^+, ArH^+, N_2H^+, HCO_2^+$ and HOC^+) are generated (Matta et al., 2013). The most efficient cooling mechanisms for electrons interacting with the 23 other model species result from:

- inelastic collisions with CO_2 due to vibrational interactions (Delgarno, 1969)

$$L_{e-\mathrm{CO_2}\ \mathrm{vibration}} = 3.35 \times 10^{-14} n_e n_{\mathrm{CO_2}} (T_e - T_n) T_e^{-0.5} \tag{A12}$$

- inelastic collision with CO_2 due to rotation interactions (Henry and McElroy, 1968)

$$L_{e-\mathrm{CO_2}\ \mathrm{rotation}} = 5.8 \times 10^{-14} n_e n_{\mathrm{CO_2}} (T_e - T_n) T_e^{-0.5} \tag{A13}$$

- inelastic fine structure interactions with O (Stubbe and Varnum, 1972)

$$L_{e-\mathrm{O}\ \mathrm{finestructure}} = 3.4 \times 10^{-12} n_e n_o \left(1 - 7 \times 10^{-5} T_e\right) \frac{T_e - T_n}{T_n} \tag{A14}$$

- elastic collisions with CO_2 (Schunk and Nagy, 1978)

$$\begin{aligned} L_{e-\mathrm{CO_2}} &= 1.27 \\ &\quad \times 10^{-6} \left(\frac{128 k_B T_e m_e}{\pi}\right)^{0.5} n_e n_{\mathrm{CO_2}} k_B (T_e - T_n) \frac{q_{d-\mathrm{CO_2}}}{m_{\mathrm{CO_2}}} \end{aligned} \tag{A15}$$

- and elastic collisions with ions (Banks and Kockarts, 1973)

$$L_{e-i} = \sum_i 3.9 \times 10^{18} (2\pi m_e)^{0.5} n_e n_i e^4 k_B (T_e - T_i) \frac{\ln \Lambda}{m_i (k_B T_e)^{1.5}} \tag{A16}$$

where $n_{\mathrm{CO_2}}$ and n_{O} and are the neutral CO_2 and O densities in cm^{-3}, respectively; T_n and T_i are the neutral and ion temperature in Kelvin, respectively; m_i and $m_{\mathrm{CO_2}}$ and are the ion and CO_2 mass in g, respectively; $q_{d-\mathrm{CO_2}}$ is the momentum average collision cross-section defined above, e is the electron charge in esu and $\ln \Lambda$ is the unitless coulomb logarithm that is ~15 for Mars. Individual loss rates are summed to represent the total loss term in the electron energy calculations.

A.2. Ions

In this work, all ions are singly charged. The expression used for ion thermal conductivity is (Schunk and Nagy, 2009):

$$\lambda_i = 3.1 \times 10^4 \frac{T_i^{2.5}}{m_i^{0.5} \left[1 + \frac{5}{4} \sum_{t \neq i} \frac{\nu_{it}}{\nu_{ii}} \left(D_{it} + 1.5 \frac{\mu_{it}}{m_i}\right)\right]} \tag{A17}$$

where T_i and m_i are as previously defined. The summation in the denominator is over all other species (ions and neutrals); ν_{ii} and ν_{it} are the ion–ion and ion–species collision frequencies in s^{-1}, respectively, described further below; D_{it} is a constant that depends on the collision type and μ_{it} is the ion–species reduced mass in g given by $m_i \times m_t/(m_i + m_t)$.

$$\nu_{ii} = 1.27 n_i \frac{\sqrt{m_i/2}}{m_i T_i^{1.5}} \tag{A18}$$

where T_i, m_i and n_i are as previously defined. The ions can interact with two other populations: (i) neutrals and (ii) other ions. For ion–neutral interactions, the collision frequency ν_{it} and constant D_{it} become ν_{in} and D_{in}, respectively. For ion–ion interactions, the subscripts change to become ν_{ij} and D_{ij}, respectively. The expressions for these parameters are (Banks, 1966; Schunk and Nagy, 2009):

$$\nu_{in} = 2.6 \times 10^{-9} n_n \sqrt{\frac{p_o}{\mu_{in}}} \tag{A19}$$

$$D_{in} = \frac{3m_i^2 + m_n^2 + \frac{8}{5} m_i m_n}{(m_i + m_n)^2} \tag{A20}$$

$$\nu_{ij} = \frac{16\sqrt{\pi}}{3} n_i m_j \frac{e^4 \ln \Lambda}{(m_i + m_j) \left(2k_B \frac{T_{ij}}{\mu_{ij}}\right)^{1.5} \mu_{ij}^2} \tag{A21}$$

$$D_{ij} = \frac{3m_i^2 + \frac{1}{10} m_i m_j - \frac{1}{5} m_j^2}{(m_i + m_j)^2} \tag{A22}$$

where p_o is the polarizability is in units of $10^{-24}\ \mathrm{cm}^3$ and is listed in Table A1; μ_{in} and μ_{ij} are the ion–neutral and ion–ion reduced masses, respectively; and T_{ij} is the reduced temperature in Kelvin given by $(m_i T_i + m_j T_j)/(m_i + m_j)$ (Schunk and Nagy, 2009).

Ions can be heated by collisions with warmer particles. The heating rate for ions resulting from energy transferred due to collisions with electrons as given by Banks and Kockarts (1973) is:

$$Q_i = 4\sqrt{2\pi m_e} n_e n_i e^4 k_B (T_e - T_i) \frac{\ln \Lambda}{m_i (k_B T_e)^{1.5}} \tag{A23}$$

where all ions are singly charged, and the terms are as previously defined.

Table A1
Polarizability from Lide (1995).

Species	Polarizability ($10^{-24}\ \mathrm{cm}^3$)
CO_2	2.91
CO	1.95
O	0.802
N_2	1.74
Ar	1.64
H	0.667
H_2	0.802

The cooling of an ion due to collisions with a colder particle is represented as a cooling rate. When an ion collides with a warmer particle, the cooling rate becomes a heating rate and is represented by the same expression with a change is sign. The cooling/heating rates from the different types of collisional interactions that ions undergo are:

- collisions with other neutral species (Banks, 1966)

$$L_{in} = 6.8 \times 10^{-13} n_i n_n (T_i - T_n) \frac{\sqrt{p_o \mu_{in}}}{m_i + m_n} \tag{A24}$$

- non-resonant collisions with other ions (Banks, 1966)

$$L_{ij} = 2.18 \times 10^{-5} n_i n_j (T_i - T_j) \frac{\ln \Lambda}{m_i m_j \left(\frac{T_i}{m_i} + \frac{T_j}{m_j}\right)^{1.5}} \tag{A25}$$

- and resonant collisions with other ions of the same species (Banks, 1966)

$$L_{ii} = 1.3 \times 10^{-4} n_i (T_i - T_n) \nu_i \tag{A26}$$

where ν_i is the collision frequency in s^{-1} of the resonant collision given by Banks (1966):

$$\nu_i = \frac{4}{3} n_n q_i \sqrt{\frac{8k_B}{\pi m_n}(T_i + T_n)} \tag{A27}$$

q_i is the average momentum collision cross-section in cm^2 given by Banks (1966):

$$q_i = 10^{-16}[A + 3.96B - B\log(T_i + T_n)]^2 \tag{A28}$$

A and B are species-specific coefficients taken from Banks (1966) and references therein.

References

Anicich, V., 1993. A survey of bimolecular ion–molecule reactions for use in modeling the chemistry of planetary atmospheres, cometary comae, and interstellar clouds: 1993 supplement. Astrophys. J. 84, 215–315.

Arkani-Hamed, J., 2004. A coherent model of the crustal magnetic field of Mars. J. Geophys. Res. 109, E09005. http://dx.doi.org/10.1029/2004JE002265.

Baille, P., Chang, J., Claude, A., Hobson, R., Ogram, G., Yau, A., 1981. Effective collision frequency of electrons in noble gases. J. Phys. B: Atom. Mol. Phys. 14, 1485–1495.

Banks, P., 1966. Collision frequencies and energy transfer: Ions. Planet. Space Sci. 14, 1105–1122.

Banks, P., Kockarts, G., 1973. Aeronomy. Academic, San Diego, Calif..

Chen, R.H., Nagy, A.F., 1978. A comprehensive model of the Venus ionosphere. J. Geophys. Res. 83 (A3), 1133–1140.

Chen, R.H., Cravens, T.E., Nagy, A.F., 1978. The martian ionosphere in light of the Viking observations. J. Geophys. Res. 83 (A8), 3871–3876. http://dx.doi.org/10.1029/JA083iA08p03871.

Choi, Y.W., Kim, J., Min, K.W., Nagy, A.F., Oyama, K.I., 1998. Effect of the magnetic field on the energetics of Mars ionosphere. Geophys. Res. Lett. 25 (14), 2753–2756.

Cravens, T.E., Gombosi, T.I., Kozyra, J., Nagy, A.F., Brace, L.H., Knudsen, W.C., 1980. Model calculations of the dayside ionosphere of Venus: Energetics. J. Geophys. Res. 85 (A13), 7778–7786.

Cui, J., Yelle, R., Müller-Wodarg, I., Lavvas, P., Galand, M., 2011. The implications of the H_2 variability in Titan's exosphere. J. Geophys. Res. 116, A11324. http://dx.doi.org/10.1029/2011JA016808.

Delgarno, A., 1969. Inelastic collisions at low energies. Can. J. Chem. 47, 1723–1729.

Forget, F. et al., 1999. Improved general circulation models of the martian atmosphere from the surface to above 80 km. J. Geophys. Res. 104, 24155–24176.

Fox, J.L., 2003. Effect of H_2 on the martian ionosphere: Implications for atmospheric evolution. J. Geophys. Res. 108 (A6), 1223. http://dx.doi.org/10.1029/2001JA000203.

Fox, J.L., Zhou, P., Bougher, S.W., 1996. The martian thermosphere/ionosphere at high and low solar activities. Adv. Space Res. 17, 203–218.

Galand, M., Moore, L., Charnay, B., Mueller-Wodarg, I., Mendillo, M., 2009. Solar primary and secondary ionization at Saturn. J. Geophys. Res. 114, A06313. http://dx.doi.org/10.1029/2008JA013981.

Hanson, W.B., Mantas, G.P., 1988. Viking electron temperature measurements: Evidence of a magnetic field in the martian ionosphere. J. Geophys. Res. 93 (A7), 7538–7544.

Hanson, W.B., Santatani, S., Zuccaro, D.R., 1977. The martian ionosphere as observed by the Viking Retarding Potential Analyzers. J. Geophys. Res. 82 (28), 4351–4363. http://dx.doi.org/10.1029/JS082i028p04351.

Henry, R.J.W., McElroy, M.B., 1968. In: Brandt, J.C., McElroy, M.B. (Eds.), The Atmospheres of Venus and Mars. Gordon and Breach Sci. Publ., London, pp. 251–279.

Herman, J.R., Hartle, R.E., Bauer, S.J., 1971. The dayside ionosphere of Venus. Planet. Space Sci. 19, 443–460.

Hunton, D.E., Viggiano, A.A., Morris, R.A., Paulson, J.F., Smith, D., Adams, N.G., 1991. The $O^+ + CO_2$ reaction: New results and atmospheric implications. J. Geophys. Res. 96 (A8), 13881–13886. http://dx.doi.org/10.1029/91JA01175.

Johnson, R.E., 1978. Comment on ion and electron temperatures in the martian upper atmosphere. Geophys. Res. Lett. 5 (11), 989–992.

Krasnopolsky, V., 2002. Mars' upper atmosphere and ionosphere at low, medium, and high solar activities: Implications for evolution of water. J. Geophys. Res. 107 (E12), 5128. http://dx.doi.org/10.1029/2001JE001809.

Lewis, S.R. et al., 1999. A climate database for Mars. J. Geophys. Res. 104, 24177–24194.

Lide, D., 1995. CRC Handbook of Chemistry and Physics, 76th ed. CRC Press Inc., Florida.

Mantas, G.P., Hanson, W.B., 1979. Photoelectron fluxes in the martian ionosphere. J. Geophys. Res. 84 (A2), 369–385. http://dx.doi.org/10.1029/JA084iA02p00369.

Mantas, G.P., Hanson, W.B., 1985. Evidence of solar wind energy deposition into the ionosphere of Mars. J. Geophys. Res. 90 (A12), 12057–12064. http://dx.doi.org/10.1029/JA090iA12p12057.

Mantas, G.P., Hanson, W.B., 1987. Analysis of martian ionosphere and solar wind electron gas data from the planar Retarding Potential Analyzer on the Viking spacecraft. J. Geophys. Res. 92, 8559–8569. http://dx.doi.org/10.1029/JA092iA08p08559.

Matta, M., Withers, P., Mendillo, M., 2013. The composition of Mars' topside ionosphere: Effects of hydrogen. J. Geophys. Res.. http://dx.doi.org/10.1002/jgra.50104.

Mendillo, M., Lollo, A., Withers, P., Matta, M., Pätzold, M., Tellmann, S., 2011. Modeling Mars' ionosphere with constraints from same-day observations by Mars Global Surveyor and Mars Express. J. Geophys. Res. 116, A11303. http://dx.doi.org/10.1029/2011JA016865.

Moore, L., Galand, M., Mueller-Wodarg, I., Yelle, R., Mendillo, M., 2008. Plasma temperatures in Saturn's ionosphere. J. Geophys. Res. 113, A10306. http://dx.doi.org/10.1029/2008JA013373.

Ness, N. et al., 2000. Effects of magnetic anomalies discovered at Mars on the structure of the martian ionosphere and solar wind interaction as follows from radio occultation experiments. J. Geophys. Res. 105, 15991–16004.

Nier, A.O., McElroy, M.B., 1976. Structure of the neutral upper atmosphere of Mars – Results from Viking 1 and Viking 2. Science 194, 1298–1300.

Roboz, A., Nagy, A.F., 1994. The energetics of Titan's ionosphere. J. Geophys. Res. 99 (A2), 2087–2093.

Rohrbaugh, R.P., Nisbet, J.S., Bleuler, E., Herman, J.R., 1979. The effect of energetically produced O_2^+ on the ion temperatures of the martian thermosphere. J. Geophys. Res. 84 (A7), 3327–3338. http://dx.doi.org/10.1029/JA084iA07p03327.

Schunk, R.W., Nagy, A.F., 1978. Electron temperatures in the *F* region of the ionosphere: Theory and observations. Rev. Geophys. 16 (3), 355–399.

Schunk, R.W., Nagy, A.F., 1980. Ionospheres of the terrestrial planets. Rev. Geophys. 18, 813–852. http://dx.doi.org/10.1029/RG018i004p00813.

Schunk, R.W., Nagy, A.F., 2009. Ionospheres, second ed. Cambridge University Press, New York.

Shimizu, M., Ashihara, O., 1972. Electron temperature in the martian ionosphere. Publ. Astron. Soc. Jpn. 24, 201–212.

Shinagawa, H., Cravens, T.E., 1989. A one-dimensional multispecies magnetohydrodynamic model of the dayside ionosphere of Mars. J. Geophys. Res. 94 (A6), 6506–6516. http://dx.doi.org/10.1029/JA094iA06p06506.

Singhal, R.P., Whitten, R.C., 1988. Thermal structure of the ionosphere of Mars: Simulations with one- and two-dimensional models. Icarus 74, 357–364.

Stubbe, P., Varnum, W.S., 1972. Electron energy transfer rates in the ionosphere. Planet. Space Sci. 20, 1121–1126. http://dx.doi.org/10.1016/0032-0633(72)90001-3.

Tobsika, W.K., Bouwer, S.D., 2006. New developments in SOLAR2000 for space research and operations. Adv. Space Res. 37 (2), 347–358. http://dx.doi.org/10.1016/j.asr.2005.08.015, ISSN 0273-117.

Walter, C.W., Cosby, P.C., Peterson, J.R., 1993. Rovibrational product distributions of O_2^+ from the reaction of $O^+(^4S)$ with CO_2. J. Chem. Phys. 98, 2860–2871.

Woods, T.N. et al., 2005. Solar EUV Experiment (SEE): Mission overview and first results. J. Geophys. Res. 110, A01312. http://dx.doi.org/10.1029/2004JA010765.